COMPUTATION OF PROPELLER TIP VORTEX FLOW

LEI LIU

Computation of Propeller Tip Vortex Flow

by

©Lei Liu
St. John's, Newfoundland, Canada

B.Eng., Dalian University of Technology, China (2004)
M.Eng., Dalian University of Technology, China (2006)

A thesis submitted to the
School of Graduate Studies
in partial fulfillment of the
requirements for the degree of
Master of Engineering

Faculty of Engineering and Applied Science
Memorial University of Newfoundland

April 2009

Abstract

The steady tip vortex flow of a marine propeller governed by Reynolds-Averaged Navier Stokes (RANS) equations was numerically simulated. The RANS equations were solved by a commercial RANS code, ANSYS-CFX. The $k - \epsilon$ turbulence model and the shear stress transport (SST) turbulence model were applied in the computation. A spiral-like computational domain was set up as one blade-to-blade passage with two side/periodic boundaries. The grid was formed by following the inlet flow angle so that the clustered grid can be aligned with the tip vortex.

Validation studies had been carried out for a uniform flow past the rotating David Taylor propeller model. In the computation, the effect of grid resolution was first investigated. Three computational grids with different minimum Jacobian, minimum volume and minimum skew angle were used. The $k - \epsilon$ and the SST turbulence models were then applied. The numerical results were validated by comparing with the experimental results and other numerical solutions. It has been demonstrated that the CFX RANS solver with two-equation turbulence models is able to predict the viscous tip vortex flow accurately. The effect of the $k - \epsilon$ and the SST turbulence models on the solution is insignificant.

Acknowledgements

I would like to thank my supervisor, Dr. Wei Qiu, who suggested my research topic, enhanced my interest in Marine Hydrodynamics, and gave me support both on the knowledge and spirit when needed. His advice and guidance have been invaluable to the development of this work.

I also wish to express my deep appreciation to the Natural Sciences and Engineering Research Council (NSERC) of Canada, Defence Research and Development Canada (DRDC) Atlantic, Oceanic Consulting Corporation through a DND/NSERC Research Partnership program, and the Graduate Study Fellowship. This work would not have been completed without their financial support.

Many thanks are extended to my colleagues and friends at the Advanced Marine Hydrodynamics Laboratory (AMHL), Qingyong Yang, Min Zhang and Chao Guo, for their useful discussions and suggestions at various stages of the work. I also would like to acknowledge the advice from Dr. Shaoyu Ni and Hui Yin.

Finally, I would like to give my special thanks to my parents, Zhiying Chen and Xilin Liu. I am profoundly grateful for their love, support and understanding.

Contents

List of Figures

List of Tables

Nomenclature

$\mathbf{B}$ Bezier curve function

D diameter of propeller

k turbulent kinetic energy

p pressure

R radius of propeller

r radial coordinate

S strain rate

$\mathbf{U}$ velocity vector

U_{in} inflow velocity in the stationary frame

U_{total} inflow velocity in the rotating frame

V_c secondary velocity

V_s primary velocity

y^+ non-dimensional wall distance

α grid distribution factor

β grid stretching factor

δ_k index angle of blade

ϵ turbulent dissipation rate

ν_t turbulence viscosity

ω specific dissipation rate/turbulence frequency

ρ water density

τ_w shear stress on the wall

Acronyms

BSL   Baseline

CFD   Computational fluid dynamics

DNS   Direct numerical simulation

LDV   Laser doppler velocimeter

LES   Large eddy simulation

RANS   Reynolds averaged Navier Stokes

RPS   Revolution per second

SST   Shear stress transport

Chapter 1

Introduction

1.1 Background and Motivation

The propeller cavitation is of major concern for ships in terms of reduced performance, erosion and passenger comfort due to cavitation induced vibrations and noise. Large efforts on experimental and numerical studies have been made on the investigation of cavitation inception and the accurate prediction of the cavitation behavior of a propeller to avoid or control the tip vortex cavitation.

Experimental studies can explore many detailed features of the tip vortex flow around a marine propeller configuration using advanced flow visualization and non-intrusive measurement techniques. However, due to the limitation of experimental measurements, some physical measurements such as the pressure

Figure 1-1: Cavitation flow of a propeller (DGA-DCE)

field in the tip vortex core, which is crucial to the prediction of cavitation inception, still remains relatively unknown. Numerical studies should be considered for predicting the tip vortex flow field.

In early years, numerical studies were not extensively utilized due to the limitations of computational resources. With the development of computer technology, computational methods are paid more attention. In this decade, numerical simulation approaches, such as direct numerical simulations (DNS) and large eddy simulations (LES), have been applied in the analysis of flow. The computational fluid dynamics (CFD) methods which solve the Reynolds Averaged Navier Stokes (RANS) equations are most appealing.

It is well known that the geometry of a marine propeller is very complex with variable section profiles, chord lengths and pitch angles. Meanwhile, to reduce the cavitation and pressure pulses on the ship's stern, higher skewness is usually applied in the design for the propeller at high rotation speed. All aspects mentioned above make the numerical simulation challenging, especially in gridding the computational domain. Appropriate grids have to be created to obtain accurate prediction for the propeller tip vortex flow. The complex geometry also causes a strong non-equilibrium boundary layer near the blade wall. This makes the turbulence modeling another challenge for numerical simulation of the propeller tip vortex flow.

1.2 Literature Review

Many numerical studies have been performed to predict the propeller cavitation by solving the RANS equations. Remarkable progress has been achieved in RANS research. Abdel-Maksoud and Heinke (2002) predicted the velocity distribution in the gap region of a ducted propeller using the commercial RANS code, CFX-TASCflow. Abdel-Maksoud et al. (2004) analyzed the effect of the hub cap shape on propeller performance using the same code. Wang et al. (2003) presented an analysis of the 3D viscous flow field around an axisymmetric body with an integrated ducted propulsor. Simonsen and Stern (2005) computed the

2

hull-rudder-propeller interaction by coupling RANS and potential codes. However, the computation of tip vortex flow of open marine propellers is limited. Hsiao and Pauley (1999) computed the steady-state tip vortex flow using NASA's RANS code INS3D-UP. Rhee and Joshi (2003) presented the computations of marine propeller flow using the commercial RANS code, FLUENT. Qiu et al. (2003) computed the tip vortex flows of various propellers using INS3D-UP. These studies showed the feasibility and advantage of the CFD method for marine propeller flow.

The complexity in the mesh generation is one of the main obstacles for numerical simulations. In order to accurately trace the tip vortices over a distance, such regions need high grid resolution. Inaccuracy of the predicted flow field is often attributed to inadequate discretization of the computation domain. Both structured and unstructured grids were used for the tip vortex flow in previous studies. Hsiao and Pauley (1999) and Qiu et al. (2003) employed an H-type structured grid to compute the tip vortex flow of the DTMB 5168 propeller with grid concentration at the vortex core. About two million grids were used in the computation domain of one blade to blade passage for the open-water condition. The general characteristics of the propeller flow were well predicted although an overly diffusive and dissipative tip vortex was obtained in computation. Rhee and Joshi (2003) used hybrid unstructured grids for the same propeller where prismatic cells were used in the boundary layer and tetrahedral cells were distributed in the computational domain far from solid boundaries. A good agreement was found for axial and tangential velocity components behind the propeller. While the predicted radial velocity component was less accurate.

Another challenge for numerical simulations is turbulence modeling. The flows off the propeller blades are dominated by strong rotation in the vicinity of the tip vortices. The strong non-equilibrium boundary layer in the propeller flow requires the turbulence models to have the ability to handle the turbulence in the tip vortex region. The algebraic turbulence models based on isotropic eddy viscosity are inadequate to treat such flows since the algebraic equation used to compute the turbulent viscosity no longer works for the high non-isotropic boundary layer

in the tip vortex region. Some one-equation and two-equation models, which have higher order of complexity and the ability to model the tip vortex flow, have been tested in previous studies. Hsiao and Pauley (1999) and Qiu et al. (2003) applied a one-equation algebraic turbulence model on fine grids to compute the tip vortex flow of a marine propeller. The discrepancy between the computational results and experimental data indicated that viscosity within the tip vortex was over predicted and it led to an overly diffusive and dissipative tip vortex. Kim and Rhee (2004) computed the tip vortex flow of a finite-span wing with Spalart-Allmaras one equation model, $k - \epsilon$ model, $k - \omega$ model and Reynolds stress transportation model. The Spalart-Allmaras model and Reynolds stress transportation model gave better predictions than the two equation eddy-viscosity models for wing tip vortex flow. Studies on the impact of various turbulence models have not been carried out for the tip vortex flow of marine propellers.

1.3 Thesis Contents

In this thesis, the uniform flow past a rotating marine propeller was computed by solving the RANS equations. The DTMB 5168 propeller was selected for the present study. Based on the work of Qiu et al. (2003), a structured grid was generated in one blade-to-blade passage computational domain for the tip vortex computation. A commercial RANS code, ANSYS-CFX was used with the $k - \epsilon$ turbulence model and the shear stress transport (SST) turbulence model. Computational results were analyzed and validated against the experimental data measured by Chesnakas and Jessup (1998), the numerical results of Hsiao and Pauley (1999), and the results computed by Qiu et al. (2003). The impact of the $k - \epsilon$ and the SST turbulence models on the solution was also discussed for the tip vortex flow of marine propeller.

The thesis is organized as follows: Chapter 2 outlines the grid generation method. In Chapter 3, the governing equations for propeller tip vortex flow are presented and the turbulence models are briefly described. Boundary conditions applied in the computation are also explained in this chapter. The numerical

4

results of tip vortex flow filed around the propeller are presented in Chapter 4. Conclusions and the future work are given in Chapter 5.

Chapter 2

Grid Generation

The grid quality is very important in the computation of the turbulent flow around propellers. Grids of poor quality can introduce errors and cause serious difficulties in convergence. Due to the complexity of tip vortex flow generated by marine propellers, the following issues have to be considered in the grid generation. Firstly, it is necessary to have a fine grid to adequately resolve the tip vortex. Hsiao and Pauley (1999) suggested that at least 15 grid points across the tip vortex core should be used to obtain a reliable near-field tip vortex for a marine propeller. Hally and Watt (2002) investigated the effect of grid density on the evolution of a laminar vortex. They found that the computed results tended to match the theoretical solutions as the number of cells across the vortex core increased. Secondly, the grid density on the propeller blade surface must be sufficient so that boundary layer effects can be well predicted. Thirdly, grids must be smooth throughout the computational domain. Finally, the grid generator has to be computationally efficient for routine applications. A gird generation program, PropGrid, developed by Qiu et al. (2003) based on the work of Hsiao and Pauley (1999), is summarized in this Chapter.
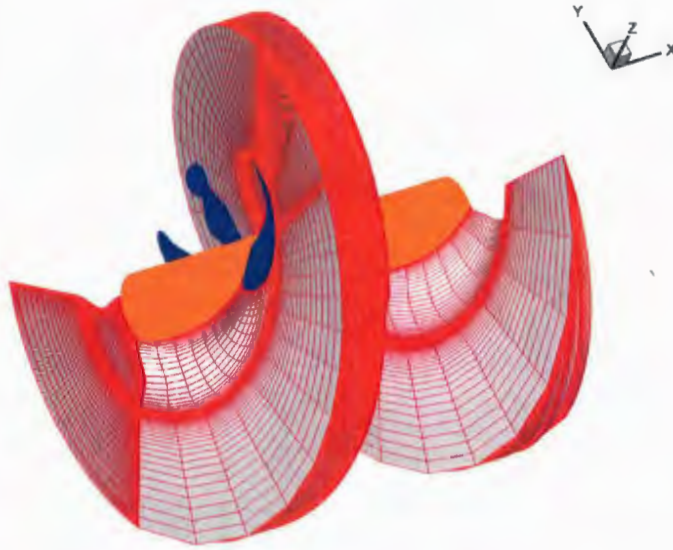
Figure 2-1: Computational domain for propeller

2.1 Computational Domain for Propellers

Since the intersection of the hub and the blade root area of the propeller blade is overly complicated, some geometry simplifications are made in the grid generation. The blade flange, root fillers and a root trailing edge cut-out are ignored. Propeller blades are assumed to be mounted on a cylindrical hub with constant radius.

Based on the work of Hsiao and Pauley (1999) and Qiu et al. (2003), the computational domain is set up as one spiral-like blade-to-blade passage with two periodic boundaries by following the inlet flow angle. This two periodic boundaries contain the suction side of a blade and the pressure side of the next blade. As shown in Figure 2-1, the other boundaries for this computational domain include the inlet boundary upstream, the outlet boundary downstream, the inner boundary located on the hub surface and the outer boundary in the spanwise direction. The advantage of this kind of computational domain is that the clustered grid can be easily aligned with the tip vortex and the flow across the periodic boundaries can be minimized.
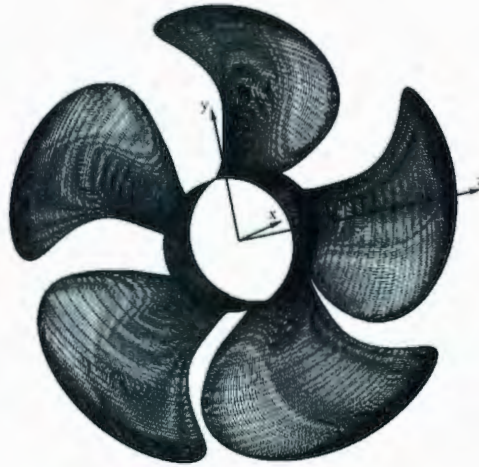
7

Figure 2-2: Cartesian coordinate system

The grid is first generated on the blade and hub surfaces with clusters at blade tip and root as well as leading and trailing edges. On the periodic boundary, grids are created in three regions: the region above the tip from the leading edge to the trailing edge, the region from the inlet boundary to the leading edge, and the region from the trailing edge to the outlet boundary. A two-dimensional grid between the blades is then created on constant radius surfaces based on the blade surface grid. Each two-dimensional grid is generated using an algebraic scheme and an elliptic smoothing routine. The three-dimensional initial grid is set up by stacking all the two-dimensional grids. An elliptic smoothing routine is applied to smooth the three-dimensional initial grid finally.

2.2   Coordinate System

A cartesian coordinate system, $oxyz$, is applied on the propeller with the positive x-axis defined as downstream direction and y-axis located at any desired angular orientation relative to the key blade. The z-coordinate is determined by the right-handed system (see Figure 2-2).

A cylindrical system is defined with the angle θ measured clockwise from the z-axis when viewed in the direction of positive x-axis. The radial coordinate, r, is
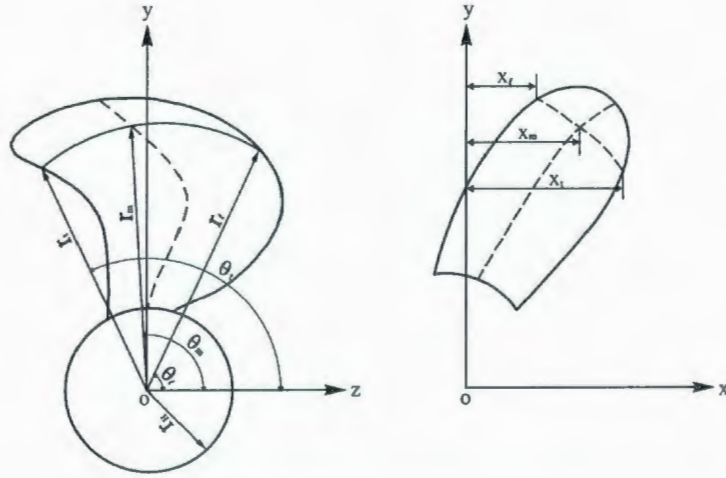
8

Figure 2-3: Cylindrical coordinate system

give by

$$r = \sqrt{y^2 + z^2} \tag{2.1}$$

A projected view of a blade form upstream is shown in Figure 2-3. In the figure, r_H is the hub radius, θ is the skew angle measured from the z-axis at radius r.

The geometry information of the propeller, i.e. leading edge, trailing edge and blade section surface, can be described mathematically both in the Cartesian and Cylindrical coordinate systems. The leading and trailing edges of blade can be constructed by passing a helix of pitch angel, $\phi(r)$, through the mid-chord line. If the expanded chord length of blade section is $c(r)$, the leading and trailing edge coordinates can be described as

$$x_{l,t} = x_m \mp \frac{c}{2} \sin \phi(r) \tag{2.2}$$

$$\theta_{l,t} = \theta_m \mp \frac{c}{2r} \cos \phi(r) \tag{2.3}$$

$$y_{l,t} = r \sin \theta_{l,t} \tag{2.4}$$

$$z_{l,t} = r \cos \theta_{l,t} \tag{2.5}$$

where the subscripts l and t denote the leading and trailing edges, respectively.

As shown in Figure 2-4, the blade section surface is defined by the functions
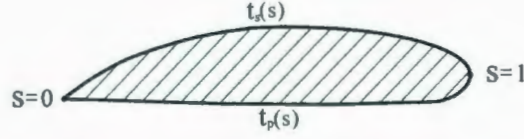
9

Figure 2-4: Blade section surface

$t_s(s)$ and $t_p(s)$ for the suction side and the pressure side of the blade, respectively. In the functions, s is a nondimensional chordwise coordinate,which is zero at the leading edge and one at the trailing edge. The function $t_s(s)$ and $t_p(s)$ are measured in a cylindrical surface of radius r in a direction normal to the helical coordinate.

A blade index angle δ_k is defined to generalize the results to all blades other than the key blade:

$$\delta_k = \frac{2\pi(k-1)}{K}, k = 1, 2, \cdots, K \qquad (2.6)$$

where K is the number of blades and k is the index of any blade. The key blade is defined by the $k = 1$. The coordinates of a point on the pressure and suction surface of a section on kth blade can be written as

$$x_{s,p} = x_m + c(s - \frac{1}{2})sin\phi - t_{s,p}cos\phi \qquad (2.7)$$

$$\theta_{s,p} = \theta_m + c(s - \frac{1}{2})\frac{cos\phi}{r} - t_{s,p}\frac{sin\phi}{r} + \delta_k \qquad (2.8)$$

$$y_{s,p} = rsin\theta_{s,p} \qquad (2.9)$$

$$z_{s,p} = rcos\theta_{s,p} \qquad (2.10)$$

where the subscripts s and p denote the suction side and the pressure side surfaces, respectively. $t_{s,p}$ is the section surface as shown in Figure 2-4.

The propeller blade surface can then be written in terms of a set of organized points. This set of organized points can be obtained by a parametric representation of blade surface (Qiu et al., 2003).

10

2.3 Grid Generation on the Blade

The computational domain in Figure 2-1 starts with the generation of the surface grid on the blade. The grids on the blade surface can be distributed based on the set of organized points. The grids shrink into a point at the blade tip. This type of grid is called an O-type grid, which is not desirable for the computation. A redistribution process has been developed to generate H-type grids on the blade surface. Figure 2-5 demonstrates the difference between O-type and H-type grids. In the H-type grid, the grid lines are curvilinear, approaching a set of horizontal and vertical lines in a pseudo-orthogonal configuration, with a topology that can be associated to the letter H.

To maintain the accuracy of the geometry definition, the number of the O-type gird points on the blade has to be increased from the original input geometry before the H-type grid is created. The number of refined grid points are set as 251 in spanwise and 141 in chordwise in the grid generation program. The procedure for creating an H-type grid from an O-type grid on the blade surface is illustrated in Figure 2-6. The H-type grid is obtained by redistributing the grid points in the tip region.

In order to simulate the tip vortex flow, it is desirable to distribute an H-type grid on the blade surface with clusters at tip and root, as well as the leading edge and the trailing edge. In PropGrid, the distribution of the H-type grid is controlled by the number of grid points in the spanwise and chordwise directions as well as the distribution functions.

The controlling function for grid points concentrated at two ends in the spanwise or chordwise direction is defined by

$$\phi(\xi) = \frac{(2\alpha + \beta)[(\beta + 1)/(\beta - 1)]^{(\xi - \alpha)/(1-\alpha)} + 2\alpha - \beta}{(2\alpha + 1)\{1 + [(\beta + 1)/(\beta - 1)]^{(\xi - \alpha)/(1-\alpha)}\}} \tag{2.11}$$

$$\psi(\zeta) = \frac{(2\alpha + \beta)[(\beta + 1)/(\beta - 1)]^{(\zeta - \alpha)/(1-\alpha)} + 2\alpha - \beta}{(2\alpha + 1)\{1 + [(\beta + 1)/(\beta - 1)]^{(\zeta - \alpha)/(1-\alpha)}\}} \tag{2.12}$$

where α and β are the gird distribution factor and stretching factor, respectively.

11
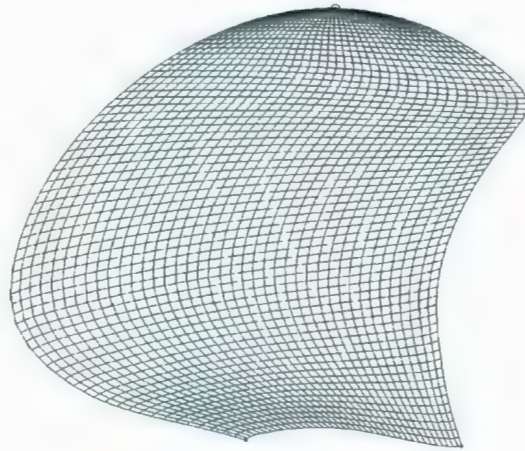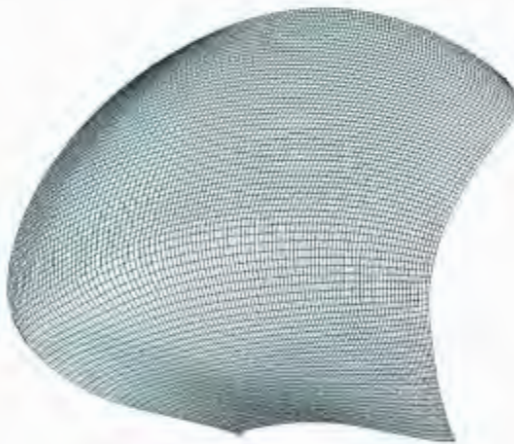
(a) *O*-type grid

(b) *H*-type grid

Figure 2-5: *O*-type and *H*-type grids
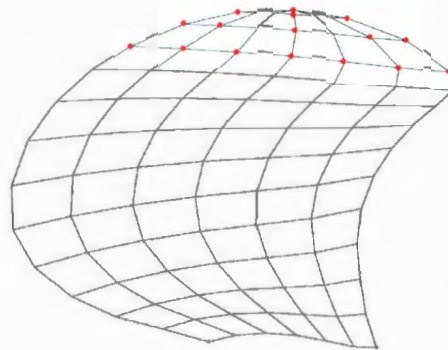
(a) *O*-type panel points
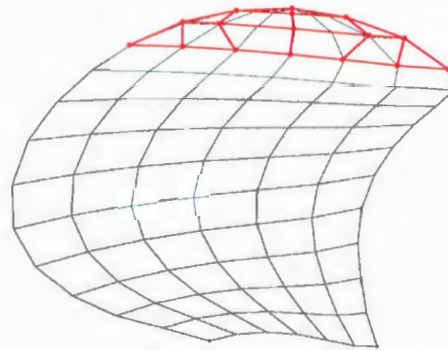
(b) Intermediate grid in the tip region
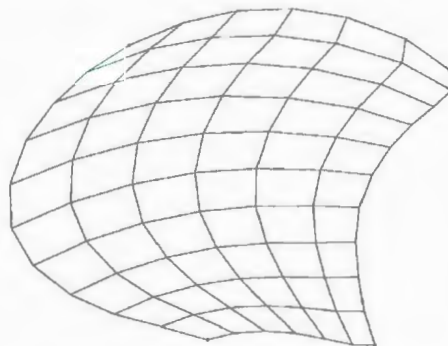
(c) Redistributed *H*-type panel

Figure 2-6: Redistributing the *O*-type panel points around the tip region (Qiu et al.,2003)

When $\alpha = 0.5$, the grid will cluster evenly at both the tip and root regions in the spanwise direction or the leading and trailing edges in the chordwise direction. The stretching factor, β, should be greater than one. The larger the value, the less concentration of grid points at end edge will be achieved. In another words, the grid will be more uniformly distributed. The intermediate variables, ϕ and ψ, are defined on the unit intervals, ξ and ζ. In the program, $\xi = \frac{I-1}{N-1}$ and $\zeta = \frac{J-1}{M-1}$, where I or J is the order of the point in the chordwise direction or the spanwise direction, N or M is the total number of points in the chordwise direction or the spanwise direction. The location of a grid point on the surface can be controlled by adjusting the single valued function $\phi(\xi)$ in the chordwise direction or $\psi(\zeta)$ in the spanwise direction.

The controlling function for grid points concentrated at one end in the spanwise or chordwise direction is defined by

$$\phi(\xi) = \frac{(\beta+1) - (\beta-1)[(\beta+1)/(\beta-1)]^{1-\xi}}{[(\beta+1)/(\beta-1)]^{1-\xi} + 1} \tag{2.13}$$

$$\psi(\zeta) = \frac{(\beta+1) - (\beta-1)[(\beta+1)/(\beta-1)]^{1-\zeta}}{[(\beta+1)/(\beta-1)]^{1-\zeta} + 1} \tag{2.14}$$

For the grid distribution on the blade surface, there are three types of clusters are provided by the program in the spanwise direction:

Type 1. Grid concentrated at the tip

Type 2. Grid concentrated at both the tip and the root

Type 3. In the spanwise direction, the blade surface is subdivided into two regions. In each region, one-end or two-end controlling function is applied

In the chordwise direction, two types of grid clusters are provided:

Type 1. Grid concentrated on both the leading edge and the trailing edge

Type 2. In the chordwise direction, the blade surface is subdivided into two regions. In each region, one-end or two-end controlling function is applied

14
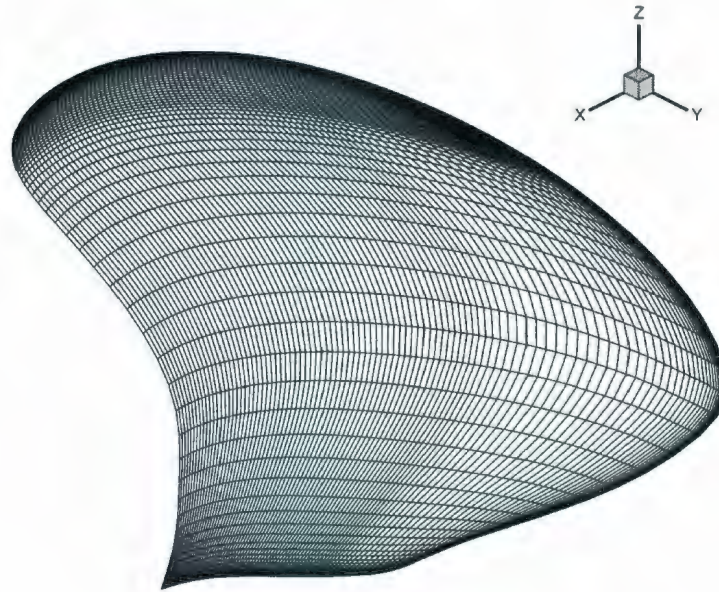
Figure 2-7: Grid distribution on the blade surface

Figure 2-7 presents the grid on the blade surface grid distribution using Type 3 and Type 2 grid distribution mentioned above in the spanwise and chordwise directions, respectively. In this figure, the total number of grid point in the spanwise direction and the chordwise direction are set as 81 and 101. The blade surface is subdivided into two regions in the spanwise direction. The first region is from $s = 0$ (root) to $s = 0.9$, where s is the non-dimensional arclength. The two-end grid distribution is applied in this region. The second region is from $s = 0.9$ to $s = 1$ (tip), where the one-end grid concentration is set. The distribution factor, α, and the stretch factor, β, are set as 0.68 and 1.05, respectively. The grid stretch factor in the second region is 1.13. In the chordwise direction, two regions are divided at $s = 0.45$ from the leading edge. In the region close to the leading edge, the number of grid points is 40 , α and β are set as 0.68 and 1.48. In the other chordwise region, the one-end stretch factor is 1.68.

(a) Region 1

(b) Region 2

(c) Region 3

Figure 2-8: Grid generation on the periodic boundary

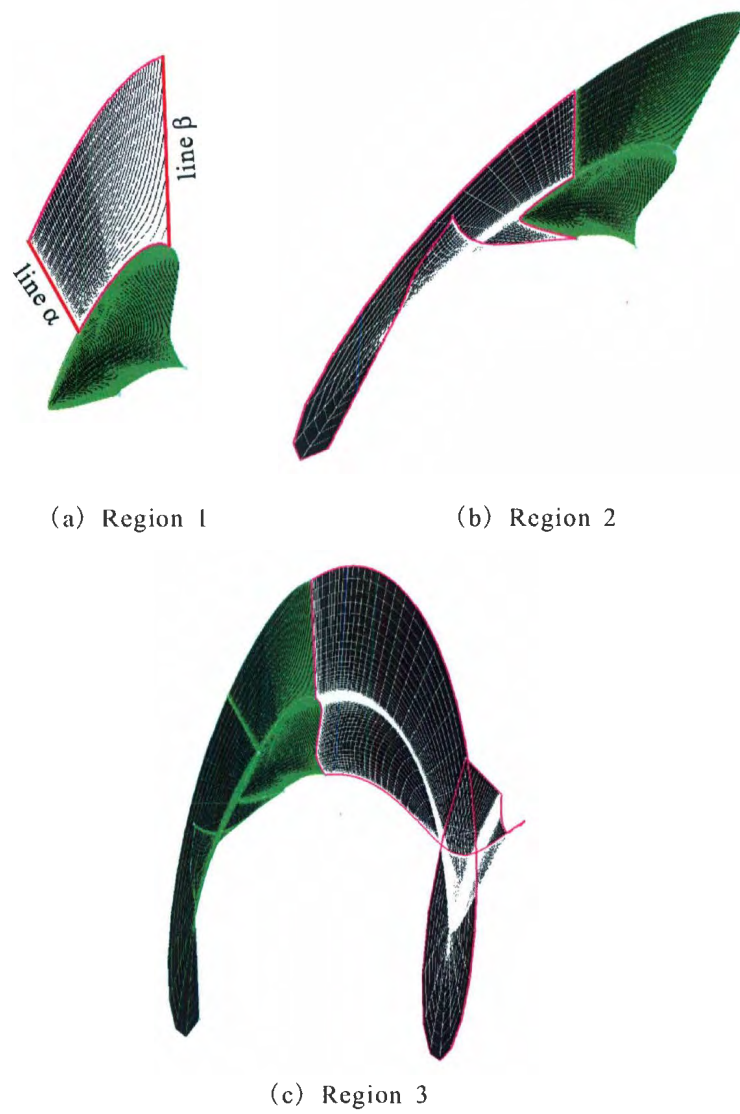## 2.4   Grid Generation on the Periodic Boundaries

After the surface grid generation on the blades, the grid is generated on the
periodic boundaries containing the suction side of one blade and the pressure side
of the next blade. The procedure to generate the periodic boundary is illustrated
in Figure 2-8. As shown in the figure, grids have to be created in three regions:
the region above the tip from the leading edge to the trailing edge (Region 1),
the region from the inlet boundary to the leading edge (Region 2), and the region
from the trailing edge to the outlet boundary (Region 3).

The grids in Region 1 are generated based on the grids at the propeller tip.
The coordinate, θ, keeps constant at each station in the chordwise direction and
the r is increased from the radius at the tip to the outer boundary. In Regions 2
and 3, the coordinates of grid are computed based on the grid information at the
leading edge and trailing edge. The rotation speed of propeller and free stream
velocity are also employed to generate the grid following the inlet flow angle.

To generate the grids in the Region 1, the following equation is used:

$$x(i,k) = x(i, KTIPNUM)$$

$$r(i,k) = r_{tip}(i) + \phi(k)\frac{r_{far} - r_{tip}(i)}{r_{tip-far}}$$

$$\theta(i,k) = \theta(i, KTIPNUM) \tag{2.15}$$

$$y(i,k) = r(i,k)sin[\theta(i,k)]$$

$$z(i,k) = r(i,k)cos[\theta(i,k)]$$

where, $k = KTIPNUM + 1, KMAX$; $i = ILE, ITE$. In the equation 2.15, ILE
and ITE are the indices of grid points on the leading edge and the trailing edge,
respectively, $KTIPNUM$ is the number of grid points on the blade surface in the
spanwise direction, $KMAX$ is the total number of grid points on the boundary
in the spanwise direction, $\phi(k)$ is the controlling function in the radial direction,
$x(i, KTIPNUM)$, $\theta(i, KTIPNUM)$ and $r_{tip}(i)$ are the x, θ and r-coordinates at
the tip.

17

To generate the grids in the Region 2, the following equation is used:

$$x(i,k) = x(ILE,k) - \frac{\phi(i)}{d_{LE}}[x(ILE,k) - x_{LE}]$$

$$r_\theta(k) = [x(ILE,k) - x_{LE}]\frac{2\pi r'(k)n}{U_\infty}$$

$$\theta(i,k) = \theta(ILE,k) + \frac{\phi(i)}{d_{LE}}\frac{r_\theta(k)}{r'(k)} \qquad (2.16)$$

$$y(i,k) = r(i,k)sin[\theta(i,k)]$$

$$z(i,k) = r(i,k)cos[\theta(i,k)]$$

where, $i = ILE - 1, 1, -1$; $k = 1, KMAX$. In the equation 2.16, $\phi(i)$ is the controlling function in the helix line direction, d_{LE} is the distance from the inlet boundary to the leading edge on the tip, x_{LE} is the x-coordinate of the inlet boundary, U_∞ is the inflow velocity, n is the RPS of the propeller, $r'(k)$ is the radius of the grid on the line α (see Figure 2-8), $x(ILE,k)$, $\theta(ILE,k)$ and $r(ILE,k)$ are the x, θ and r-coordinates on the leading edge.

For the Region 3, the following equation is used:

$$x(i,k) = x(ITE,k) + \frac{\phi(i)}{d_{TE}}[x_{TE} - x(ITE,k)]$$

$$r_\theta(k) = [x_{TE} - x(ITE,k)]\frac{2\pi r'(k)n}{U_\infty}$$

$$\theta(i,k) = \theta(ITE,k) + \frac{\phi(i)}{d_{TE}}\frac{r_\theta(k)}{r'(k)} \qquad (2.17)$$

$$y(i,k) = r(i,k)sin[\theta(i,k)]$$

$$z(i,k) = r(i,k)cos[\theta(i,k)]$$

where, $i = ITE + 1, IMAX$; $k = 1, KMAX$. In the equation 2.17, $\phi(i)$ is again the controlling function in the helix line direction, d_{TE} is the distance from the trailing edge to the outlet boundary on the tip, x_{TE} is the x-coordinate of outlet boundary, $r'(k)$ is the radius of the grid on the line β (see Figure 2-8), $x(ITE,k)$,
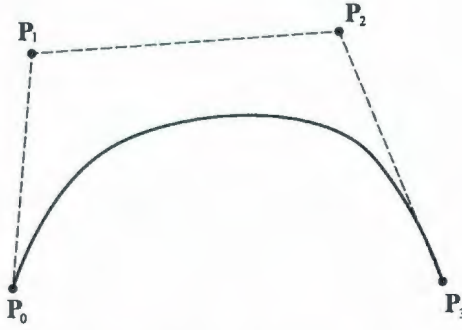
Figure 2-9: Cubic Bezier curve

$\theta(ITE, k)$ and $r(ITE, k)$ are the x, θ and r-coordinates on the trailing edge.

2.5 Initial Grid Generation

After the grid generation on the blade surfaces and periodic boundaries is completed, a two-dimensional grid between the blades is then created on each constant radius surface based on the blade surface grid and the first grid spacings. On each constant radius surface, a Bezier curve (Faux and Pratt, 1979) is used to define a grid line between two boundaries. The cubic Bezier curve in three-dimensional is applied in the program.

$$\mathbf{B}(t) = (1-t)^3 \mathbf{P}_0 + 3t(1-t)^2 \mathbf{P}_1 + 3t^2(1-t)\mathbf{P}_2 + t^3 \mathbf{P}_3 \qquad (2.18)$$

where $0 \le t \le 1$. The curve starts at $\mathbf{P}_0$ toward $\mathbf{P}_1$, and arrives at $\mathbf{P}_3$ coming from the direction of $\mathbf{P}_2$ as shown in Figure 2-9.

The points on the Bezier curve are distributed by using the two-end controlling function. The application of Bezier curves assures that the grid is normal to the blade surface where the boundary condition of zero normal pressure gradient is applied. After creating the grid on each constant radius surface, each two-dimensional grid is smoothed by applying a two-dimensional elliptic smoothing routine.

2.6 Elliptic smoothing Technique

An elliptic smoothing routine is used to smooth the gird which is generated by using linear internal interpolation. The elliptic smoothing routine generates grids by solving a set coupled Poisson elliptic partial differential equations. The equations are given below for the three-dimensional case which can be simplified to a two-dimensional case:

$$\xi_{xx} + \xi_{yy} + \xi_{zz} = \overline{P}(\xi, \eta, \zeta)$$

$$\eta_{xx} + \eta_{yy} + \eta_{zz} = \overline{Q}(\xi, \eta, \zeta) \qquad (2.19)$$

$$\zeta_{xx} + \zeta_{yy} + \zeta_{zz} = \overline{R}(\xi, \eta, \zeta)$$

In RANS solvers, the RANS equations on structured grids are usually transformed in to generalized coordinates by

$$\xi = \xi(x, y, z)$$

$$\eta = \eta(x, y, z) \qquad (2.20)$$

$$\zeta = \zeta(x, y, z)$$

The Jacobian of the transformation is computed by

$$J = \det \frac{\partial(\xi, \eta, \zeta)}{\partial(x, y, z)} = \begin{vmatrix} \xi_x & \xi_y & \xi_z \\ \eta_x & \eta_y & \eta_z \\ \zeta_x & \zeta_y & \zeta_z \end{vmatrix} = \begin{vmatrix} x_\xi & x_\eta & x_\zeta \\ y_\xi & y_\eta & y_\zeta \\ z_\xi & z_\eta & z_\zeta \end{vmatrix}^{-1} \qquad (2.21)$$

where $\xi_x = \frac{\partial \xi}{\partial x}$, $x_\xi = \frac{\partial x}{\partial \xi}$, etc.

The metric terms are calculated as

$$
\begin{pmatrix} \xi_x \\ \xi_y \\ \xi_z \end{pmatrix} = J \begin{bmatrix} y_\eta z_\zeta - y_\zeta z_\eta \\ x_\zeta z_\eta - x_\eta z_\zeta \\ x_\eta y_\zeta - x_\zeta y_\eta \end{bmatrix} = J \begin{pmatrix} \gamma_{11} \\ \gamma_{21} \\ \gamma_{31} \end{pmatrix}
$$

$$
\begin{pmatrix} \eta_x \\ \eta_y \\ \eta_z \end{pmatrix} = J \begin{bmatrix} y_\zeta z_\xi - y_\xi z_\zeta \\ x_\xi z_\zeta - x_\zeta z_\xi \\ x_\zeta y_\xi - x_\xi y_\zeta \end{bmatrix} = J \begin{pmatrix} \gamma_{12} \\ \gamma_{22} \\ \gamma_{32} \end{pmatrix} \qquad (2.22)
$$

$$
\begin{pmatrix} \zeta_x \\ \zeta_y \\ \zeta_z \end{pmatrix} = J \begin{bmatrix} y_\xi z_\eta - y_\eta z_\xi \\ x_\eta z_\xi - x_\xi z_\eta \\ x_\xi y_\eta - x_\eta y_\xi \end{bmatrix} = J \begin{pmatrix} \gamma_{13} \\ \gamma_{23} \\ \gamma_{33} \end{pmatrix}
$$

Using the Jacobian of the transformation above, Equation 2.19 can be transformed into

$$
\alpha_{11}\mathbf{r}_{\xi\xi} + \alpha_{22}\mathbf{r}_{\eta\eta} + \alpha_{33}\mathbf{r}_{\zeta\zeta} + 2(\alpha_{12}\mathbf{r}_{\xi\eta} + \alpha_{13}\mathbf{r}_{\xi\zeta} + \alpha_{23}\mathbf{r}_{\eta\zeta}) = \frac{-1}{J^2}(\overline{P}\mathbf{r}_\xi + \overline{Q}\mathbf{r}_\eta + \overline{R}\mathbf{r}_\zeta) \quad (2.23)
$$

with

$$
\mathbf{r} = \begin{pmatrix} x \\ y \\ z \end{pmatrix}
$$

$$
\alpha_{i,j} = \sum_{m=1}^{3} \gamma_{mi}\gamma_{mj}, \quad i = 1,2,3; j = 1,2,3
$$

The SOR (Successive Overrelaxation) algorithm is chosen to solve those equations.

The grid distribution can be controlled by the forcing functions $\overline{P}$, $\overline{Q}$ and $\overline{R}$. If $\overline{P} = \overline{Q} = \overline{R} = 0$, the Poisson equations reduce to Laplace equations. Based on the work by Sorenson(1989), both the first grid spacing and angel to the boundary can be specified. The forcing funtions used in the present program are defined as

$$
\overline{P}(\xi,\eta,\zeta) = \overline{p}(\xi,\zeta)e^{-\alpha\eta}
$$

$$\overline{Q}(\xi, \eta, \zeta) = \overline{q}(\xi, \zeta)e^{-\alpha\eta} \qquad (2.24)$$

$$\overline{R}(\xi, \eta, \zeta) = \overline{r}(\xi, \zeta)e^{-\alpha\eta}$$

where α is a positive constant which determines the decay rate of the grid clustering and $\overline{p}$, $\overline{q}$ and $\overline{r}$ will be determined by specifying the first grid spacing and angle to the boundary. The forcing functions must satisfy the desired spacing and orthogonality which have been specified by the initial grid distribution.

Before determining the forcing function in Equation 2.23, the partial derivatives of $\mathbf{r}$ with respect to ξ, η and ζ at the boundary, i.e. at $\eta = 0$, need to be determined first. From Equation 2.23, the partial derivatives of $\mathbf{r} = x\mathbf{i} + y\mathbf{j} + z\mathbf{k}$ can be expressed as

$$\frac{\partial \mathbf{r}}{\partial \xi} = \frac{\partial x}{\partial \xi}\mathbf{i} + \frac{\partial y}{\partial \xi}\mathbf{j} + \frac{\partial z}{\partial \xi}\mathbf{k}$$

$$\frac{\partial \mathbf{r}}{\partial \eta} = \frac{\partial x}{\partial \eta}\mathbf{i} + \frac{\partial y}{\partial \eta}\mathbf{j} + \frac{\partial z}{\partial \eta}\mathbf{k} \qquad (2.25)$$

$$\frac{\partial \mathbf{r}}{\partial \zeta} = \frac{\partial x}{\partial \zeta}\mathbf{i} + \frac{\partial y}{\partial \zeta}\mathbf{j} + \frac{\partial z}{\partial \zeta}\mathbf{k}$$

That desired spacing and orthogonality can be specified by the three relations

$$\mathbf{r}_\xi \cdot \mathbf{r}_\eta = 0$$

$$\mathbf{r}_\eta \cdot \mathbf{r}_\eta = s^2 \qquad (2.26)$$

$$\mathbf{r}_\zeta \cdot \mathbf{r}_\eta = 0$$

where s is the first grid spacing at the boundary. Equation 2.26 is expanded as

$$x_\xi x_\eta + y_\xi y_\eta + z_\xi z_\eta = 0$$

$$x_\eta x_\eta + y_\eta y_\eta + z_\eta z_\eta = s^2 \qquad (2.27)$$

$$x_\zeta x_\eta + y_\zeta y_\eta + z_\zeta z_\eta = 0$$

The first equation and the third equation in Equation (2.27) are first solved as

22

follows:

$$\begin{bmatrix} x_\xi \ y_\xi \\ x_\zeta \ y_\zeta \end{bmatrix} \begin{pmatrix} x_\eta \\ y_\eta \end{pmatrix} = \begin{pmatrix} -z_\xi z_\eta \\ -z_\xi z_\eta \end{pmatrix} \tag{2.28}$$

Cramer's rule is applied to get the solution for x_η and y_η.

$$x_\eta = \frac{-z_\eta(z_\xi y_\zeta - z_\zeta y_\xi)}{x_\xi y_\zeta - x_\zeta y_\xi} = \frac{-z_\eta \gamma_{12}}{-\gamma_{32}}$$

$$y_\eta = \frac{-z_\eta(x_\xi z_\zeta - x_\zeta z_\xi)}{-(x_\zeta y_\xi - x_\xi y_\zeta)} = \frac{-z_\eta \gamma_{22}}{-\gamma_{32}}$$

Substituting x_η and y_η into the second equation in Equation 2.27 gives

$$z_\eta = \frac{s\gamma_{32}}{\sqrt{\gamma_{12}^2 + \gamma_{22}^2 + \gamma_{32}^2}}$$

$$x_\eta = \frac{s\gamma_{12}}{\sqrt{\gamma_{12}^2 + \gamma_{22}^2 + \gamma_{32}^2}}$$

$$y_\eta = \frac{s\gamma_{22}}{\sqrt{\gamma_{12}^2 + \gamma_{22}^2 + \gamma_{32}^2}}$$

Solutions x_η, y_η and z_η give the first derivative $\mathbf{r}_\eta$. The second derivatives $\mathbf{r}_{\eta\eta}$ can be derived from the Taylor series:

$$\mathbf{r}_{\eta\eta} = \frac{-7\mathbf{r}|_{j=1} + 8\mathbf{r}|_{j=2} - \mathbf{r}|_{j=3}}{2(\triangle\eta)^2} - \frac{3\mathbf{r}_\eta|_{j=1}}{\triangle\eta} \tag{2.29}$$

where j is the index in the η direction.

To determine the values for $\bar{p}$, $\bar{q}$ and $\bar{r}$, Equation 3.30 is rewritten at $\eta = 0$ as

$$\bar{p}\mathbf{r}_\xi + \bar{q}\mathbf{r}_\eta + \bar{r}\mathbf{r}_\zeta = \mathbf{h} \tag{2.30}$$

where

$$\mathbf{h} = \begin{pmatrix} h_1 \\ h_2 \\ h_3 \end{pmatrix} = -J^2[\alpha_{11}\mathbf{r}_{\xi\xi} + \alpha_{22}\mathbf{r}_{\eta\eta} + \alpha_{33}\mathbf{r}_{\zeta\zeta} + 2(\alpha_{12}\mathbf{r}_{\xi\eta} + \alpha_{13}\mathbf{r}_{\xi\zeta} + \alpha_{23}\mathbf{r}_{\eta\zeta})]$$

This system can be solved by Cramer's rule to obtain

$$\bar{p} = (h_1\gamma_{11} + h_2\gamma_{21} + h_3\gamma_{31})/J$$

$$\bar{q} = (h_1\gamma_{12} + h_2\gamma_{22} + h_3\gamma_{32})/J \qquad (2.31)$$

$$\bar{r} = (h_1\gamma_{13} + h_2\gamma_{23} + h_3\gamma_{33})/J$$

Based on the elliptic grid scheme described above, a two-dimensional elliptic smoothing routine has been developed to smooth the two-dimensional initial grid.

2.7 Computational Grid Generation

The three-dimensional computational grid is set up by stacking all the two-dimensional initial grids, but the grid generated using linear internal interpolation is usually not smooth. An elliptic smoothing routine is used to smooth the computational gird. It first smooths the grid in the whole domain except the boundary layer region since the desired spacing and orthogonality have been assured in the computational grid generation. If there are grid cells which do not satisfy the criteria, the routine will list the information about those cells. The final spiral-like computation domain is shown in Figure 2-10.

The last step of the program is to output the grid file in the format of the ANSYS-CFX. Not only the coordinates of grid but also the element information has to be contained in the grid file for the ANSYS-CFX. To apply the boundary conditions in the ANSYS-CFX, the location of each boundary is also needed to be specified in the grid file. The whole process of the gird generation for a propeller is shown in Figure 2-11.
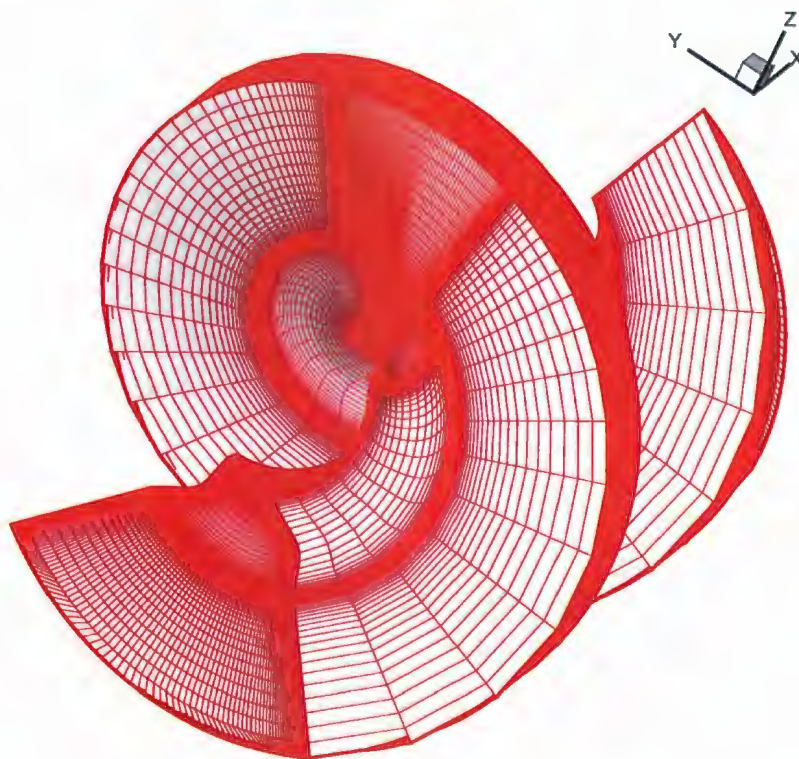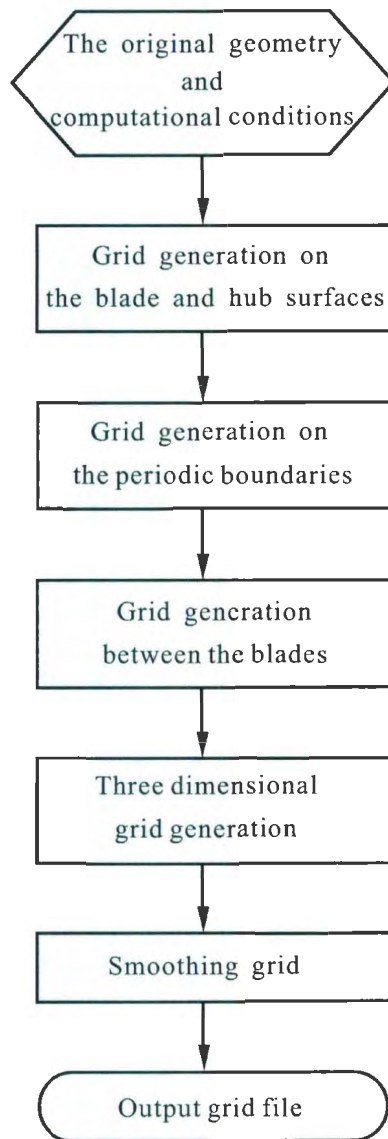
24

Figure 2-10: A spiral-like computational domain

Figure 2-11: Flow chart of the grid generation for a propeller

Chapter 3

Mathematical Formulation

3.1 Governing Equation

The Navier-Stokes (N-S) equations are the basic mathematical models to describe viscous flows around propellers in the CFD method. They are composed of the continuity equation and the momentum equations, containing variables of pressure and velocities. To numerically simulate the propeller tip vortex flow, the RANS equations, derived from the N-S equations by introducing averaged and fluctuating components for those variables, are used:

$$\frac{\partial \rho}{\partial t} + \nabla \cdot (\rho \mathbf{U}) = 0 \tag{3.1}$$

$$\frac{\partial \rho \mathbf{U}}{\partial t} + \nabla \cdot (\rho \mathbf{U} \otimes \mathbf{U}) = -\nabla p + \nabla \cdot \{\rho \nu [\nabla \mathbf{U} + (\nabla \mathbf{U})^T - \frac{2}{3}\delta \nabla \cdot \mathbf{U}]\} + \nabla \cdot (-\rho \overline{\mathbf{u} \otimes \mathbf{u}}) \tag{3.2}$$

where δ is the Kronecker delta funcion, $\rho \overline{\mathbf{u} \otimes \mathbf{u}}$ are the Reynolds stresses, which have to be modeled to enclose the governing equations, $\otimes$ is the tensor product of two vectors, $\mathbf{U} \otimes \mathbf{V}$ is defined as,

$$\mathbf{U} \otimes \mathbf{V} = \begin{bmatrix} U_x V_x & U_x V_y & U_x V_z \\ U_y V_x & U_y V_y & U_y V_z \\ U_z V_x & U_z V_y & U_z V_z \end{bmatrix}$$

27

3.2 Turbulence Models

It is well known that the RANS equations cannot be solved without information about the Reynolds stress terms. The turbulence models must be involved to enclose the governing equations in the computation. In the past four decades, many turbulence models have been specifically developed by CFD researchers to account the effects of turbulence. In general, those turbulence models can be divided into two types: eddy viscosity models and Reynolds stress models.

The eddy viscosity models mean that the Reynolds stresses are assumed to be related to the velocity gradients and turbulence viscosity by the gradient diffusion hypothesis (Boussinesq, 1877):

$$-\rho \overline{\mathbf{u} \otimes \mathbf{u}} = \rho \nu_t [\nabla \mathbf{U} + (\nabla \mathbf{U})^T] - \frac{2}{3} \delta \rho (k + \nu_t \nabla \cdot \mathbf{U}) \tag{3.3}$$

where δ is the Kronecker's delta, ν_t is the turbulence viscosity, which has to be modeled.

Turbulence models which are based on the turbulence viscosity are all called eddy viscosity models, such as the Cebeci-Smith model (Smith and Cebeci, 1967) and the Baldwin-Lomax model (Baldwin and Lomax, 1978), which are algebraic zero-equation models that give turbulence viscosity as a function of the local boundary layer velocity profile. The Baldwin-Barth model (Baldwin and Barth, 1990) and the Spalart-Allmaras model (Spalart and Allmaras, 1992) are one-equation models that solve a transport equation for a viscous variable. The $k - \epsilon$ model (Jones and Launder, 1973) and the $k - \omega$ model (Wilcox, 1988) are two-equation models that include two extra transport equations to represent the turbulent properties of the flow.

The Reynolds stress models are different from the eddy viscosity models. These models do not use the eddy viscosity hypothesis, but solve an equation for the transport of Reynolds stress. Algebraic Reynolds stress models solve algebraic equations for the Reynolds stress, whereas differential Reynolds stress models solve differential transport equations for Reynolds stress. In general, there are

three varieties of the standard Reynolds stress models (the LRR-IP, the LRR-QI and the SSG) and two varieties of Omega-Based Reynolds Stress Models (the Omega and the Baseline). The LRR-IP and LRR-QI models were developed by Launder et al. (1975). "IP" stands for Isotropization of Production, and "QI" stands for Quasi-Isotropic. In these models, the pressure-stain correlations are linear. The SSG model, developed by Speziale et al. (1991), uses a quadratic relation for the pressure-stain correlation. The Omega Reynolds stress model and the Baseline (BSL) Reynolds stress are all based on the ω-equation, which allows for a more accurate near wall treatment.

This section presents a brief description of the $k - \epsilon$ model, the $k - \omega$ model and the Shear Stress Transport (SST) model, which were used in the present computation.

3.2.1 $k - \epsilon$ model

The $k - \epsilon$ model is one of the most common two-equation turbulence models. It includes two extra transport equations for k and ϵ, where k is the turbulent kinetic energy, and ϵ is the turbulent dissipation rate. The turbulent viscosity ν_t is computed from

$$\nu_t = c_\mu \frac{k^2}{\epsilon} \tag{3.4}$$

the values of k and ϵ are solved from the differential transport equations as below.

$$\frac{\partial k}{\partial t} + \nabla \cdot (\mathbf{U}k) = \nabla \cdot [(\nu + \frac{\nu_t}{\sigma_k})\nabla k] + \nu_t P_k - \epsilon \tag{3.5}$$

$$\frac{\partial \epsilon}{\partial t} + \nabla \cdot (\mathbf{U}\epsilon) = \nabla \cdot [(\nu + \frac{\nu_t}{\sigma_\epsilon})\nabla \epsilon] + (c_{\epsilon 1}\nu_t P_k - c_{\epsilon 2}\epsilon)\frac{\epsilon}{k} \tag{3.6}$$

where the constant coefficients $c_\mu = 0.09$, $c_{\epsilon 1} = 1.44$, $c_{\epsilon 2} = 1.92$, $\sigma_k = 1.0$ and $\sigma_\epsilon = 1.3$. P_k is the turbulence production which is modeled as

$$P_k = \nabla \mathbf{U} \cdot (\nabla \mathbf{U} + \nabla \mathbf{U}^T) \tag{3.7}$$

29

For low-Reynolds number computations, the $k-\epsilon$ model would typically require a near wall resolution of $y^+ < 0.2$. While the $k-\omega$ model, which will be described in the next section, would require at least $y^+ < 2$. It leads the advantage of the $k-\omega$ for near wall treatment under low-Reynolds number. Note that y^+ is non-dimensional wall distance

$$y^+ = \frac{u_\tau y}{\nu} \tag{3.8}$$

where the frictional velocity on the wall, $u_\tau = (\tau_w/\rho)^{\frac{1}{2}}$, ρ is the fluid density, τ_w is the shear stress on the wall, $\tau_w = \nu \partial u/\partial y$.

3.2.2 $k-\omega$ model

The $k-\epsilon$ model assumes that the turbulence viscosity is linked to the turbulence kinetic energy, k, and turbulence frequency ω, via the relation:

$$\nu_t = \frac{k}{\omega} \tag{3.9}$$

The two transport equations for the k and ω are :

$$\frac{\partial k}{\partial t} + \nabla \cdot (\mathbf{U}k) = \nabla \cdot [(\nu + \frac{\nu_t}{\sigma_k})\nabla k] + \nu_t P_k - \beta' k\omega \tag{3.10}$$

$$\frac{\partial \omega}{\partial t} + \nabla \cdot (\mathbf{U}\omega) = \nabla \cdot [(\nu + \frac{\nu_t}{\sigma_\omega})\nabla \omega] + \alpha \frac{\omega}{k}\nu_t P_k - \beta\omega^2 \tag{3.11}$$

with $\alpha = 5/9$, $\beta = 0.075$, $\beta' = 0.09$, $\sigma_k = 2$ and $\sigma_\omega = 2$, and P_k is calculated as in the $k-\epsilon$ model.

3.2.3 Shear Stress Transport (SST) Model

It is well known that $k-\omega$ model have strong sensitivity to freestream conditions (Menter, 1993). Depending on the value specified for ω at the inlet, a significant variation in the results of the model can be obtained, which is undesirable. In order to solve the problem, a blending between the $k-\omega$ model near the wall

surface and the $k - \epsilon$ model in the outer region was developed by Menter (1994).

SST model combines the advantage of the $k - \omega$ model and $k - \epsilon$ model by blending function F_1. The equations of $k - \omega$ model are multiplied by function F_1, the transformed $k - \epsilon$ equations by a function $1 - F_1$. F_1 is equal to 1 near the surface and switches over to zero in side the boundary layer. In the SST model, the turbulence viscosity ν_t is formulated by

$$\nu_t = \frac{\alpha_1 k}{\max(\alpha_1 \omega, SF_2)} \tag{3.12}$$

where F_2 is again a blending function similar to F_1, S is an invariant measure of the strain rate defined by

$$S = \sqrt{2 S_{ij} S_{ij}} \tag{3.13}$$

with $S_{ij} = \frac{1}{2}(\frac{\partial U_i}{\partial x_j} + \frac{\partial U_j}{\partial x_i})$.

Two transport equations are given as

$$\frac{\partial k}{\partial t} + \nabla \cdot (\mathbf{U} k) = \nabla[(\nu + \frac{\nu_t}{\sigma_{k3}})\nabla k] + \nu_t P_k - \beta' k \omega \tag{3.14}$$

$$\frac{\partial \omega}{\partial t} + \nabla \cdot (\mathbf{U} \omega) = \nabla[(\nu + \frac{\nu_t}{\sigma_{\omega 3}})\nabla \omega] + 2(1 - F_1)\frac{\nabla k \nabla \omega}{\sigma_{\omega 2}\omega} + \alpha_3 \nu_t \frac{\omega}{k} P_k - \beta_3 \omega^2 \tag{3.15}$$

where, $\alpha_1 = 5/9$, $\alpha_2 = 0.44$, $\beta_1 = 0.075$, $\beta_2 = 0.0828$, $\beta' = 0.09$, $\sigma_{k1} = 2$, $\sigma_{k2} = 1$, $\sigma_{\omega 1} = 2$, $\sigma_{\omega 2} = 1/0.856$, $\alpha_3 = F_1 \alpha_1 + (1 - F_1)\alpha_2$, $\beta_3 = F_1 \beta_1 + (1 - F_1)\beta_2$, $\sigma_{k3} = F_1 \sigma_{k1} + (1 - F_1)\sigma_{k2}$ and $\sigma_{\omega 3} = F_1 \sigma_{\omega 1} + (1 - F_1)\sigma_{\omega 2}$.

The two blending functions are critical to the success of the method, which are given below are based on the distance to the nearest surface and on the flow variables:

$$F_1 = \tanh(t_1^4) \tag{3.16}$$

with

31

$$t_1 = \min[\max(\frac{\sqrt{k}}{\beta'\omega d}, \frac{500\nu}{d^2\omega}), \frac{4\rho k}{CD_{k\omega}\sigma_{\omega2}d^2}]$$

where d is the distance to the nearest wall, ν is the kinematic viscosity, ρ is the density of flow, and $CD_{k\omega} = \max(2\rho\nabla k\nabla\omega/\sigma_{\omega2}\omega, 1.0 \times 10^{-10})$.

$$F_2 = \tanh(t_2^2) \tag{3.17}$$

with

$$t_2 = \max(\frac{2\sqrt{k}}{\beta'\omega d}, \frac{500\nu}{d^2\omega})$$

3.3 Numerical Method

A commercial RANS code, ANSYS-CFX, was applied to solve the propeller tip vortex flow in this work. The brief description of ANSYS-CFX solver is presented below.

ANSYS-CFX solver uses a unique hybrid finite-element/ finite-volume approach to discretize RANS equations. As a finite volume method, it satisfies strict global conservation by enforcing local conservation over control volumes that are constructed around each mesh vertex or node. The finite element methodology is used to describe the solution variation (needed for various surface fluxes and source terms) within each element. Advection fluxes are evaluated using a high-resolution scheme that is essentially second-order accurate and bounded. For transient flows, an implicit second order accurate time differencing scheme is used.

In this thesis, the computations are conducted on a rotating frame. The Rotating Frames of Reference (RFR) is used to specify the computational domain that is rotating about an axis. The right-hand rule is used to determine the direction of the rotation. When the computational domain with a rotating frame is specified, the ANSYS CFX solver computes the appropriate Coriolis and centrifugal momentum terms, and solves a rotating frame total energy equation.

For the boundary conditions, inlets, outlets, openings, walls and symmetry planes are needed to be specified in ANSYS-CFX. Since the grid generation of

propeller only considered one blade-to-blade passage computational domain, a rotational periodic boundary condition is needed to account the influence of the other blades. The Fluid-Fluid Interface Modeling in ANSYS-CFX allows users to create the periodic interface boundaries. Meanwhile, ANSYS-CFX also offers various turbulence models such as the $k - \epsilon$ model, the $k - \omega$ model and the SST model.

Chapter 4

Numerical Results and Discussions

The DTMB 5168 propeller at the advance coefficient $J = 1.1$ was selected in the present study. The ANSYS-CFX with the $k - \epsilon$ turbulence model and the SST turbulence model was used to compute the flow field. The computed velocity components in the flow field and around tip vortex core were compared with the experimental results and solutions by other numerical methods. The original geometry of the suction side and the pressure side of DTMB 5168 propeller was provided in terms of three dimensional points on 51 radial stations and 17 chord fractions at each station. Table 4.1 summarizes the model geometry and operational conditions for the steady state situation.

Table 4.1: DTMB 5168 Propeller Particulars

Designation	Values
Diameter ($inch$)	15.856
Inflow velocity ($inch/s$)	421.44
Chord length at $0.7R$ ($inch$)	6.897
Advance coefficient	1.1
Rotation speed (RPS)	24.163
Combined velocity at $0.7R$ ($inch/s$)	942.12
Reynolds number	4.2×10^6

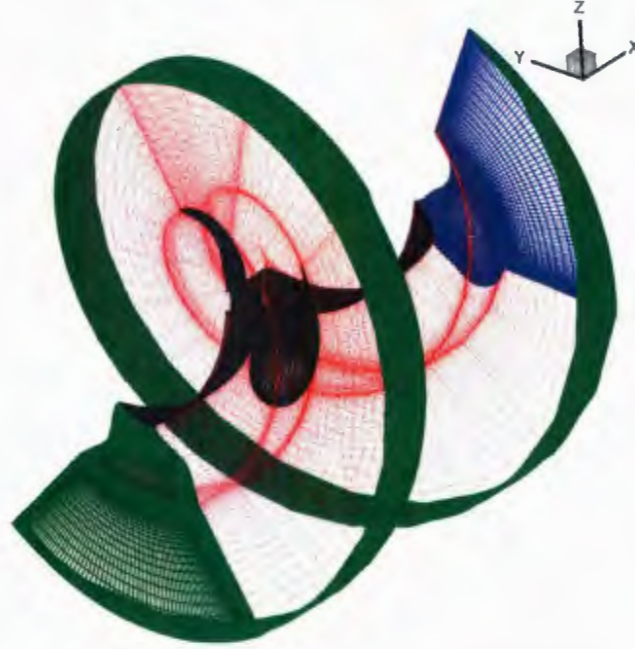In the computations, the water density and viscosity are given as $\rho_{water} =$

Figure 4-1: Boundary conditions of the computation

$997 kg/m^3$ and $\mu_{water} = 8.89 \times 10^{-4} kgm^{-1}s^{-1}$, respectively.

4.1 Boundary Conditions

The boundary conditions on each of the boundaries are specified as follows: no-slip wall condition is applied on the blades and the hub surfaces (denoted by black in the Figure 4-1). Freestream condition is applied on the inlet boundary and the outer surface in the spanwise direction (denoted by green in the Figure 4-1). The flow rate is specified at the outlet boundary (denoted by blue in the Figure 4-1). Rotational periodic conditions is applied on the periodic boundaries by the Fluid-Fluid Interface Modeling (denoted by red in the Figure 4-1).

4.2 Primary/Secondary Coordinate System

To better describe the tip vortex structure, a primary/secondary coordinates system (see Figure 4-2) is used. The the primary velocity, V_s, is defined in
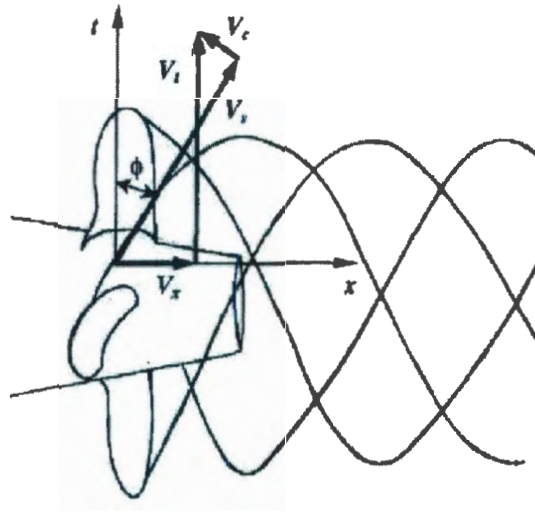
35

Figure 4-2: The primary/secondary coordinate system (Hsiao and Pauley, 1999)

the axial-tangential $x - t$ plane at the propeller pitch angle, ϕ. The secondary velocities, the tangential velocity V_c and the radial velocity V_r, are then on the secondary-flow plane which is normal to the primary velocity. Since the pitch angle varies in the radial direction, the velocity components in this coordinate system were calculated at each radial station by

$$V_s = V_x \sin(\phi(r)) + V_t \cos(\phi(r)) \tag{4.1}$$

$$V_c = -V_x \cos(\phi(r)) + V_t \sin(\phi(r)) \tag{4.2}$$

$$V_r = V_r \tag{4.3}$$

In this coordinate system, the tip vortex axis is normal to the secondary-flow plane so that the structure of vortex core can be well defined.
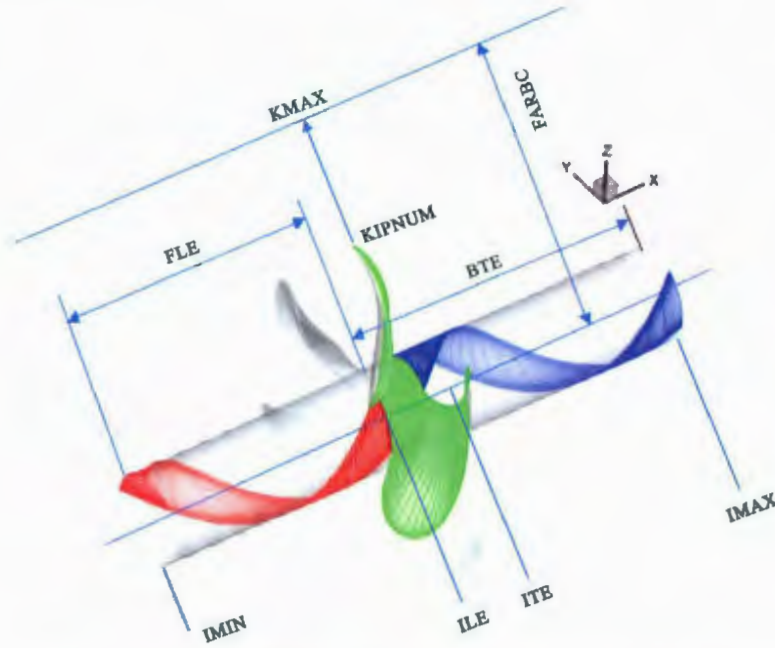
Figure 4-3: Computational domain for DTMB 5168 (Qiu et al.,2003)

4.3 Effect of the Grid Resolution

In this section, three computational grids, Grid I, Grid II and Grid III, were used to investigate the effect of the grid resolution. As shown in Figure 4-3, all the computational domains in the present study were created by setting the inlet boundary at $x_{in} = FLE \times D = -0.5D$ upstream, and the outlet boundary $x_{out} = BTE \times D = 1.0D$ downstream, where D is propeller diameter. The outer boundary in the radial direction is located at one propeller diameters (FARBC=1.0). The detailed grid information of these different computational domains is listed in the Table 4.2.

For Grid I, the first grid spacing was 3.6×10^{-4} inches and 1.236×10^{-3} inches, corresponding to y^+ =7.5, on both the blade and the hub surfaces. The total points in Grid I is about 1.92 million. For Grid II, the first grid spacing was 1.0×10^{-4} inches and 4.0×10^{-4} inches, corresponding to y^+ =2.08 and 2.43, on the blade surface and the hub surface, respectively. The total points in Grid II is about 2.37 million. For Grid III, the first grid spacing was 4.8×10^{-5} inches and

37

Table 4.2: Grids with Different Resolutions

	Grid I	Grid II	Grid III
IMAX	171	211	231
JMAX	101	101	111
KMAX	111	111	121
ILE	25	40	40
ITE	125	140	150
KTIPNUM	81	81	81
Minimum Jacobian	3.13	4.64	6.99
Minimum Volume(inch^3)	7.78×10^{-10}	4.49×10^{-12}	5.63×10^{-12}
Minimum Skew Angle(degree)	0.13	0.017	0.015

1.648×10^{-4} inches, corresponding to $y^+ = 1.0$, on both the blade and the hub surfaces. The total points in Grid III is about 3.10 million. Note that a small first grid spacing may lead to grid cells with negative Jacobian values which will cause the ANSYS-CFX solver not convergent. The value of the first grid spacing can be increased to overcome the problem. The grid quality, in terms of Jacobian, volume and skew angel, can influence the accuracy of results and the convergency.

The line plots of velocities V_x, V_t and V_r, which cross the tip vortex center on the tangential direction at the station $x = 0.2386R$ (R is the propeller radius), were compared with experimental data measured by Chesnakas and Jessup (1998) to show the effect of the grid resolution (Figures 4-4 to 4-5). The center of the vortex core is defined at the location with minimum V_s and is specified at $\theta = 0$ in the plots. As shown in these figures, the first valley of V_x and V_t corresponds to the wake and the second valley is associated with the tip vortex. In the experiment of Chesnakas and Jessup, a fiber-optic laser doppler velocimeter (LDV) system was used to obtain coincident measurement. The uncertainty within the vortex core was less than 3% of U_{in} for all measured components of the mean velocity.

All the numerical and experimental results and coordinates are nondimensionalized. The velocity components in cylinder coordinate system are nondimensionalized by the inflow velocity in the stationary frame, U_{in}, as follows:
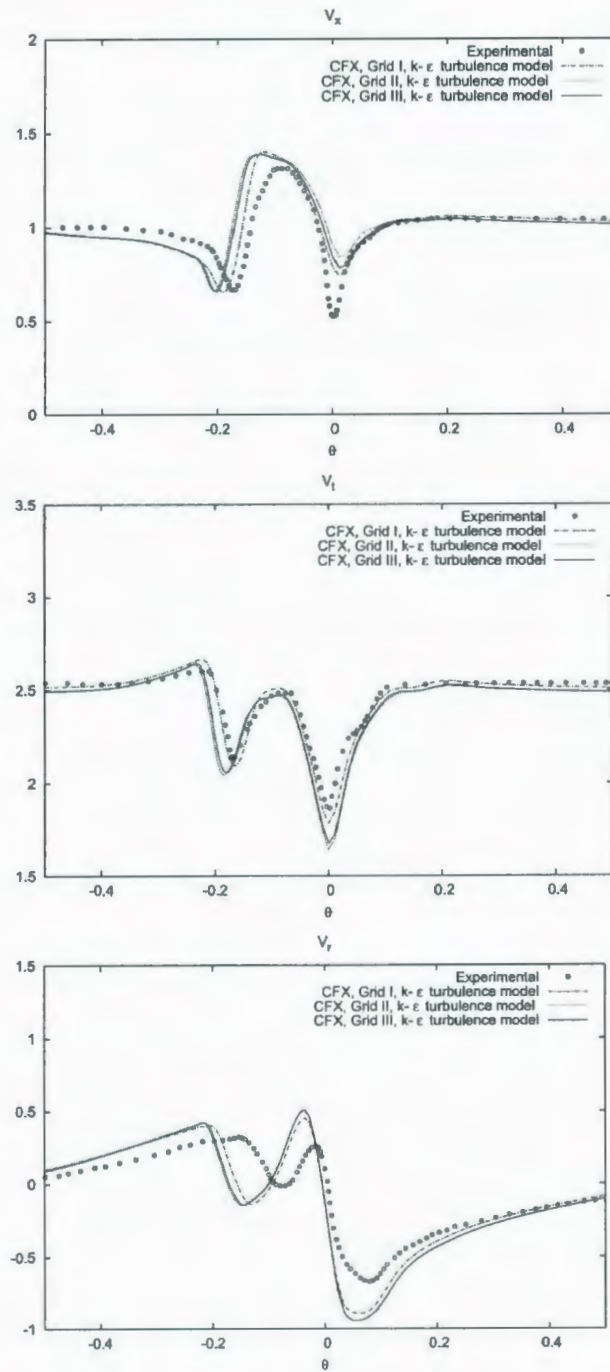
Figure 4-4: The line plot V_x, V_t, V_r across the tip vortex center in the tangential direction at $x/R = 0.2386$ with the $k - \epsilon$ turbulence model
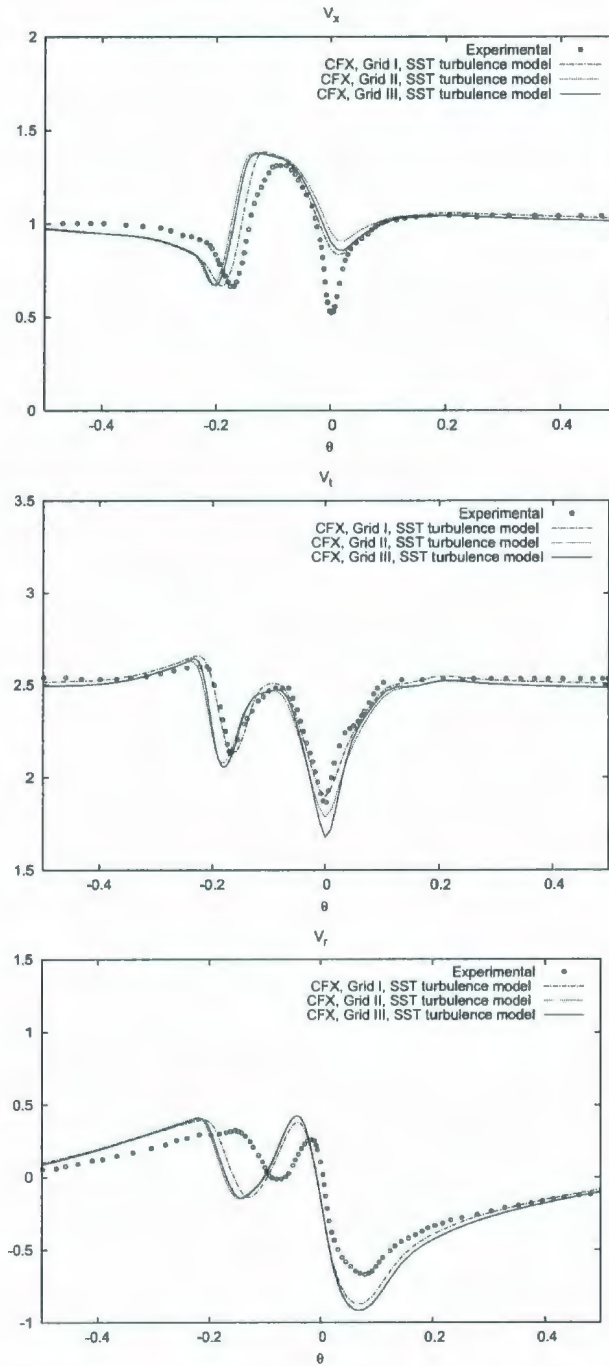
Figure 4-5: The line plot V_x, V_t, V_r across the tip vortex center in the tangential direction at $x/R = 0.2386$ with the SST turbulence model

$$V_i = \frac{V_i}{U_{in}} \qquad (4.4)$$

The spatial coordinates are nondimensionalized by the radius of the propeller, R

$$x_i = \frac{x_i}{R} \qquad (4.5)$$

In the plots of V_x, V_t and V_r with the $k - \epsilon$ turbulence model (Figure 4-4), the numerical results with Grid I gave better predictions than those with Grid II and Grid III. The same situation happened to the computed results with the SST turbulence model (Figure 4-5). Although the number of total points in Grid I was the least and the first gird spacing was the biggest as shown in Table 4.2, the values of the minimum volume and the minimum skew angle in Grid I were much bigger than the others. Note that the value of the minimum Jacobian in Grid I was the same order of magnitude with those in Grid II and Grid III. It can be observed that the quality of the grid, in terms of volume, skew angle and Jacobian, has major effect on the solution. Based on the studies above, Grid I is chosen for the following computations.

4.4 Validation Studies

In this section, the CFX numerical results with the $k - \epsilon$ turbulence model and the SST turbulence model are discussed. The contour of three computed velocity components, V_x, V_t and V_r at $x/R = 0.2386$ were compared with the experimental data in Figures 4-6 to 4-8.

From Figures 4-6 to 4-8, the computed velocity components by $k - \epsilon$ and the SST turbulence models are in good agreement with the experimental data. There are no significant difference between the results by the $k - \epsilon$ and the SST models. Only a very small difference occurs in the area near the hub for V_r (Figure 4-8). Visually, the SST model seems to give a better solution by comparing with the experimental results. An important issue in turbulence modeling is the numerical treatment of the equations in regions close to walls. The near-wall formulation
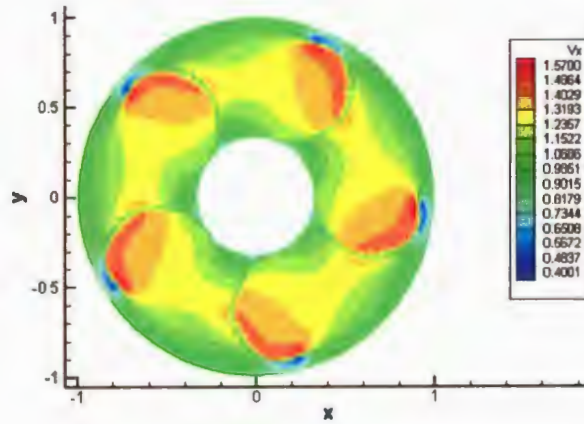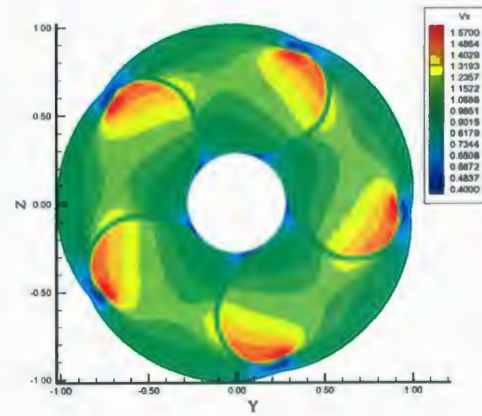
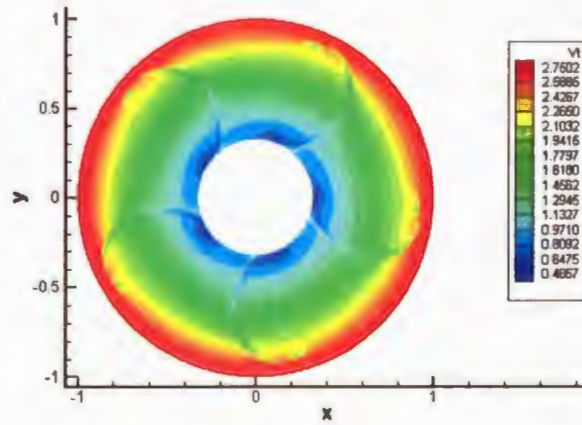(a) Experimental results by Chesnakas and Jessup (1998)
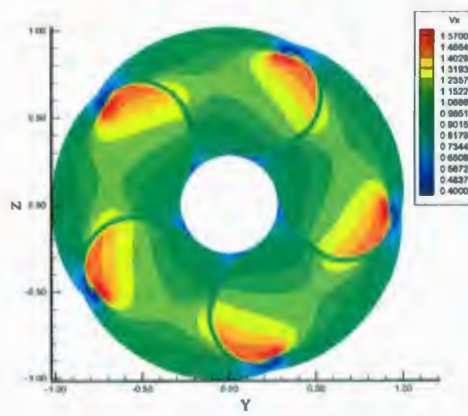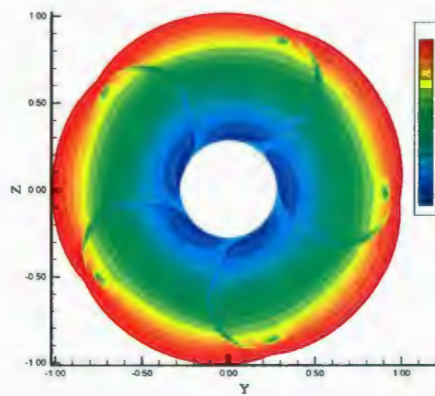

(b) $k - \epsilon$ model

(c) SST model

Figure 4-6: Axial computational velocity V_x from CFX with $k - \epsilon$ model and SST model at $x/R = 0.2386$
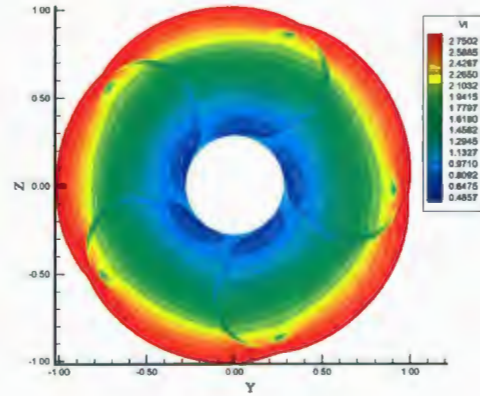
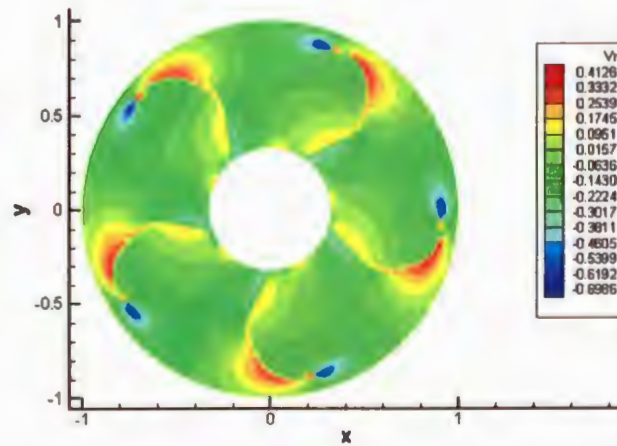(a) Experimental results by Chesnakas and Jessup (1998)
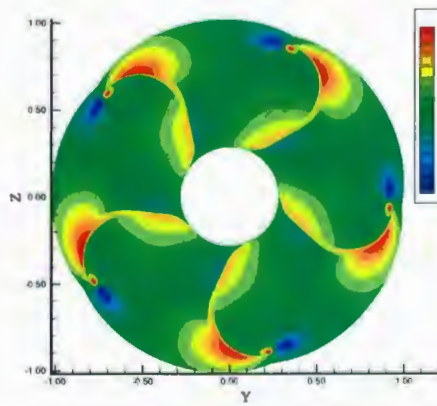

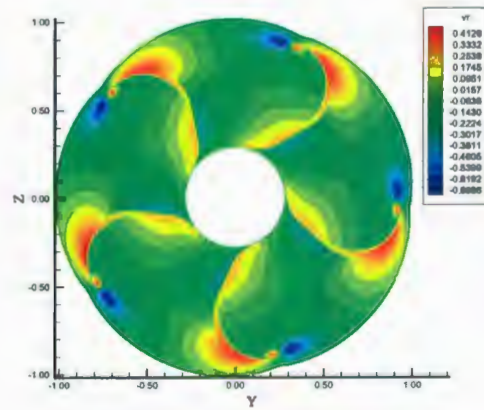(b) $k - \epsilon$ model

(c) SST model

Figure 4-7: Axial computational velocity V_t from CFX with $k - \epsilon$ model and SST model at $x/R = 0.2386$

43

(a) Experimental results by Chesnakas and Jessup (1998)

(b) $k - \epsilon$ model

(c) SST model

Figure 4-8: Axial computational velocity V_r from CFX with $k - \epsilon$ model and SST model at $x/R = 0.2386$

determines the accuracy of the wall shear stress predictions. As mentioned in the previous chapter, the SST model combined the advantage of $k - \epsilon$ model and the $k - \omega$ model. For the SST turbulence model, the new wall boundary treatment exploits the simple and robust near-wall formulation of the $k - \omega$ model and switches automatically from a low-Reynolds number formulation to a wall function treatment based on grid density.

The primary velocity V_s at $x/R = 0.2386$ were compared with the experimental data measured by Chesnakas and Jessup (1998) in Figure 4-9. The close-up view of the tip vortex core region in the primary coordinate system is given in Figure 4-10. There are about 15×20 grid points used in the tip vortex. The primary velocity V_s in the primary/secondary coordinate is non-dimensionalized by the inflow velocity in the rotating frame, U_{total}:

$$U_{total} = \sqrt{U_{in}^2 + (2\pi n r)^2} \tag{4.6}$$

where n is the rotation speed of the propeller, and $r = \sqrt{y^2 + z^2}$.

From Figures 4-9 to 4-10, it is seen that the current numerical results in general agree with the experimental data. The discrepancy between the CFX numerical results and the experimental data is likely caused by the grid resolution in the vortex core, the large first gird spacings, and the turbulence models employed. Further study on the domain size, grid resolution and effects of the turbulence models will be carried out in the next stage.

To get better quantitative comparison, the line plots of velocities V_x, V_t and V_r, which cross the tip vortex center on the tangential direction at the station $x = 0.2386R$, were compared with experimental data and other numerical results by INS3D-UP in Figure 4-11. In the work of Hsiao and Pauley (1999), the computations were carried out using INS3D-UP with a one-equation Baldwin-Barth turbulence model, and the total grids of the whole computational domain are about 2.36 million. In the work of Qiu et al. (2003), INS3D-UP with the same turbulence model was applied, and about 1.92 million grids were used. As shown in Figure 4-11, all numerical results gave reasonable prediction for the
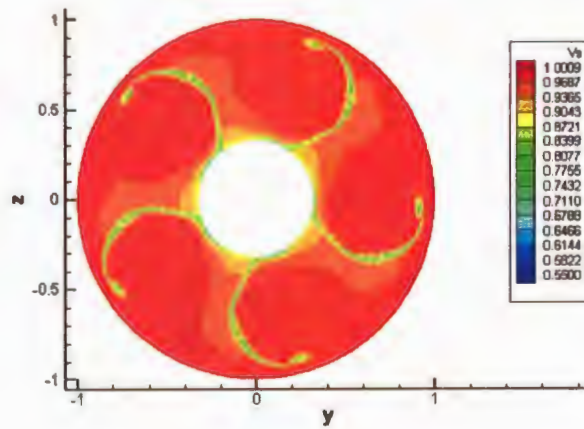
(a) Experimental results by Chesnakas and Jessup (1998)
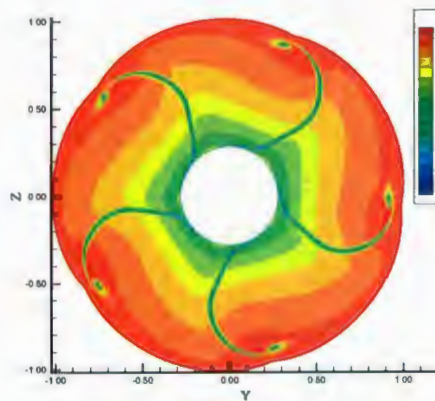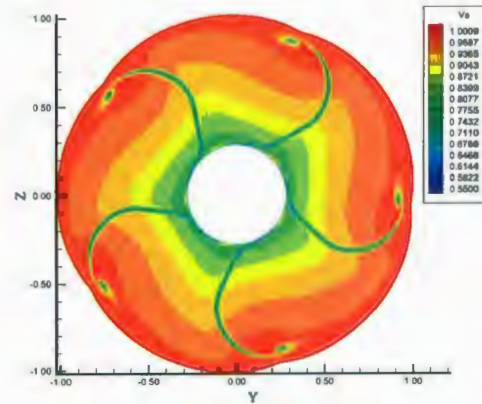
(b) $k - \epsilon$ model

(c) SST model

Figure 4-9: Axial computational velocity V_s from CFX with $k - \epsilon$ model and SST model at $x/R = 0.2386$
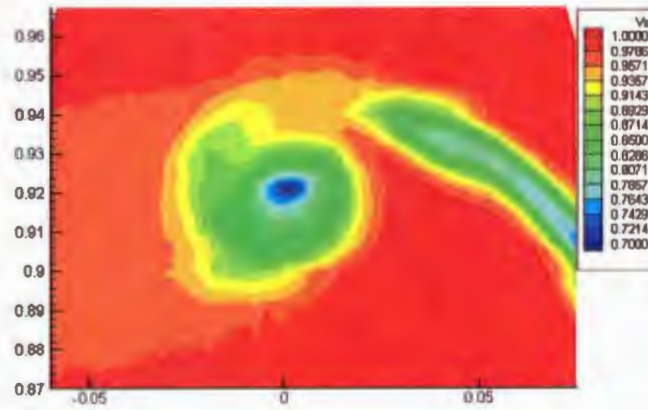
(a) Experimental results by Chesnakas and Jessup (1998)
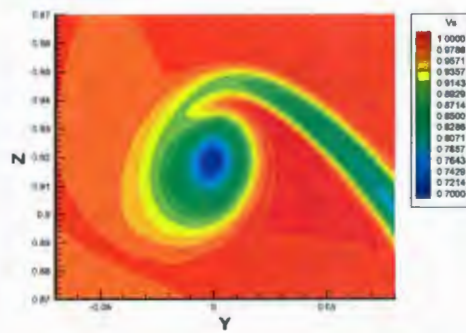
(b) $k - \epsilon$ model
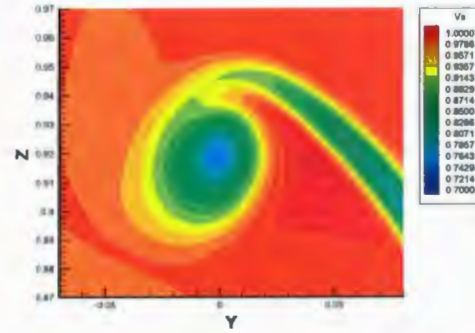

(c) SST model

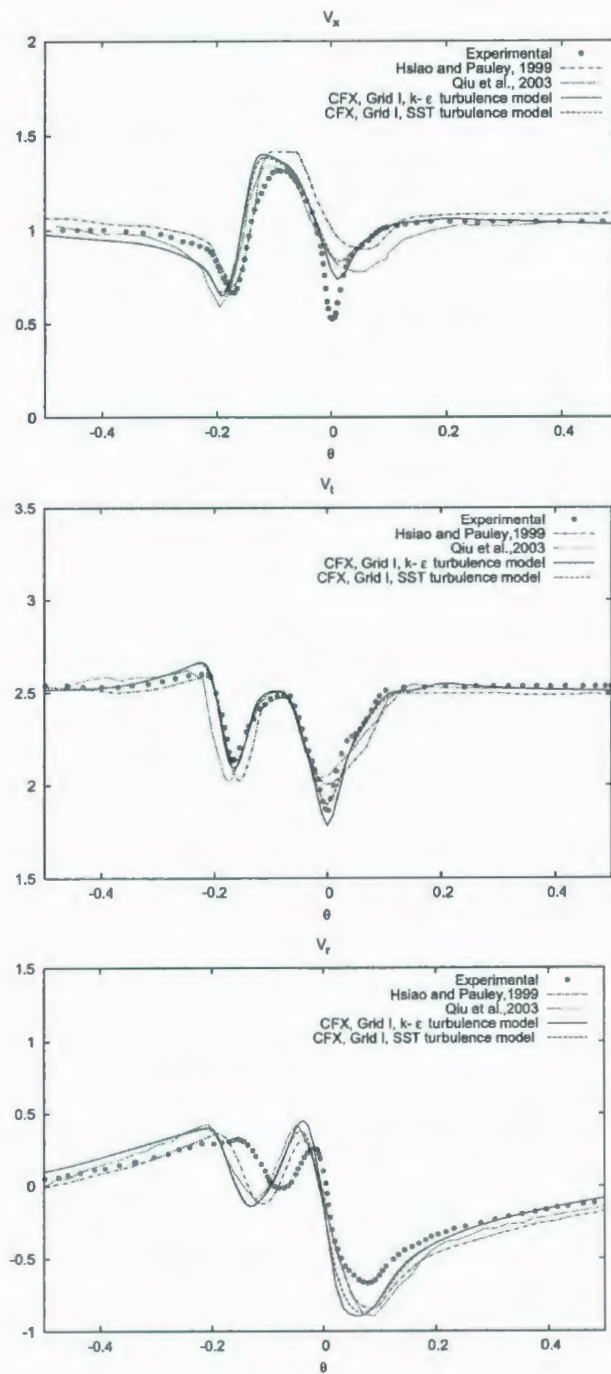Figure 4-10: Close-up view of V_s from CFX with $k - \epsilon$ model and SST model at $x/R = 0.2386$

Figure 4-11: The line plot V_x, V_t, V_r across the tip vortex center in the tangential direction at $x/R = 0.2386$

tip vortex flow.

In the plot of V_x, the numerical results by ANSYS-CFX with the $k - \epsilon$ and SST turbulence models gave better predictions of the valley shape at the vortex location, and the SST turbulence model gave relatively high values comparing with the $k - \epsilon$ turbulence model. At the wake location of V_x, Hsiao and Pauley (1999) presented very good predictions of shape and values, while the predictions by Qiu et al. (2003) were a little lower than the experimental data. The differences of computational values between the results of Qiu et al. (2003) and Hsiao and Pauley (1999) are mainly due to the less number of grids and larger first grid spacings employed in the work of Qiu et al. (2003). Note that the first grid spacings of 1×10^{-5} inches and 1×10^{-4} inches on the blade surface and the hub surface were used in the work of Hsiao and Pauley (1999), and 2.4×10^{-4} inches and 8.24×10^{-4} inches on the blade surface and the hub surface were used in the work of Qiu et al. (2003). There were about 16×20 grid points used within the tip vortex core in the work of Hsiao and Pauley (1999) and Qiu et al. (2003). The numerical results by ANSYS-CFX with the $k - \epsilon$ and SST turbulence models gave very similar solutions at the wake location, and they were both agree well with the value of experimental data.

In the plot of V_t, the results by ANSYS-CFX with the SST and $k - \epsilon$ turbulence models gave the best prediction of the tip vortex center, and the SST turbulence model gave relatively more accurate solutions than the $k - \epsilon$ turbulence model. The results by Qiu et al. (2003) and Hsiao and Pauley (1999) also agreed well with the experimental data. For V_r, all the numerical predictions in generally agree with the experimental data.

From all the comparison in this section, it can be concluded that the choice of turbulence model and the grid resolution has impact on the the prediction of tip vortex flow. All the turbulence models, the Baldwin-Barth turbulence model, the $k - \epsilon$ turbulence model and the SST turbulence model involved in the computations, fall into the class of eddy viscosity models, which relate the Reynolds stresses to the velocity gradients via the isotropic turbulent

viscosity. Since the non-isotropic effects are important in simulating the strong non-equilibrium boundary layer in the tip vortex flow, the Reynolds stresses turbulence models with an equation for the transport of Reynolds stress instead of using the eddy viscosity hypothesis should be considered in the future work.

Chapter 5

Conclusions

The viscous flow around rotating marine propellers governed by the Reynolds-Average Navier Stokes equation (RANS) was computed by the commercial code, ANSYS-CFX. In the computation, the SST and $k - \epsilon$ turbulence models were employed. A spiral-like computational grid was generated between two blades with two sides boundaries formed by following the local inlet flow angle at each radian section.

The study of the effect of the grid resolution was first carried out to investigate the quality of the control volumes, such as the minimum volume, the minimum skew angle and the minimum Jacobian, in the computational grid. It has been shown that the prediction of tip vortex flow depends on the grid quality. The grid with larger values of the minimum volume and the minimum skew angle leads to a better prediction of the tip vortex flow around the propeller.

The effect of the SST and the $k - \epsilon$ turbulence models on the solution was also discussed. There was no significant difference between the predictions by the $k - \epsilon$ and the SST models. However, in comparison with solutions by INS3D-UP with the one-equation model and different grid resolutions, it can be observed that the choice of turbulence model and the grid resolution have impact on the the prediction of tip vortex flow. From the line plots of velocities, ANSYS-CFX with the two-equation turbulence models gave better predictions of the valley shapes of wake and tip vortex core than INS3D-UP with the one-equation Baldwin-Barth

turbulence model.

Validation studies have been carried out for a David Taylor propeller model 5168. Velocity fields were computed and compared with experimental results and other numerical results. The solutions by ANSYS-CFX are generally in a good agreement with them. It has been demonstrated that the CFX RANS solver is able to predict viscous tip vortex flow problem based on the structured grid.

For future work, the Reynolds stress turbulence models should be considered in the computation. More studies should be carried out to investigate the interplay between the turbulence modeling and the grid resolution. The computation should also be extended to unsteady cases.

References

Abdel-Maksoud, M. and Heinke, H.J., 2002, Scale effects on ducted propellers, 24th Symposium on Naval Hydrodnamics, Fukuoka, Japan.

Abdel-Maksoud, M., Heinke, H.J. and Blaurock, J., 2004, Numerical and experimental investigation of the hub vortex flow of a marine propeller, 25th Symposium on Naval Hydrodynamics, St. John's, Canada.

Baldwin, B.S. and Barth, T.J., 1990, A one equation turbulence transport model for high Reynolds number wall-bounded flows, NASA Technical Memorandum 102847.

Baldwin, B.S. and Lomax, H., 1978, Thin layer approximation and algebraic model for separated turbulent flows, AIAA pp. 78-257.

Boussinesq, J., 1877, Thorie de lcoulement Tourbillant, Mem. Prsents par Divers Savants Acad. Sci. Inst. Fr., Vol. 23, pp. 46-50.

Chesnakas, C.J. and Jessup, S.D., 1998, Propeller tip vortex flow measurement using 3-component LDV, 22nd Symposium on Naval Hydrodynamics, Washington D.C., USA.

Filipiak, M., 1996, Mesh generation, Edinburgh parallel computing center, The University of Edinburgh, U.K.

Hally, D. and Watt, G.D., 2002, RANS calculations of the evolution of vortices, DREA TR 2001-216, Defence R&D Canada Atlantic, Nova Scotia, Canada.

Hsiao, C.T. and Pauley, L.L., 1999, Numerical computation of tip vortex flow generated by a marine propeller, ASME Journal of Fluids Engineering, 30(5).

Kim, S.E. and Rhee, S.H., 2004, Toward high-fidelity prediction of tip-vortex around lifting surfaces, 25th Symposium on Naval Hydrodynamics, St. John's,

Canada.

Davidson, L., 2003, An introduction to turbulence models, Publication 97/2, Department of Thermo and Fluid Dynamics, Chalmers University of Technology, Sweden.

Launder, B.E., Reece, G.J. and Rodi, W., 1975, Progress in the developments of a Reynolds-stress turbulence closure, J. Fluid Mechanics, Vol. 68, pp. 537-566.

Jones, W.P. and Launder, B.E., 1973, The calculation of low-Reynolds-number phenomena with a two equation model of turbulence. Int. J. Heat Mass Transfer 16, pp. 1119-1130.

Menter, F.R., 1993, Zonal two equation $k - \omega$ turbulence models for aerodynamic flows, AIAA Paper 93-2906.

Menter, F.R., 1994, Two-equation eddy-viscosity turbulence models for engineering applications, AIAA-Journal, Vol. 32, No. 8, PP.1598-1605.

Qiu, W. Peng, H. and Brennan, D., 2003, Development of surface geometry and external flow field gridding software for the computation of propeller surface and tip vortex flow - final report, DRDC Atlantic CR2003-91, Defence R&D Canada Atlantic, Nova Scotia, Canada.

Rhee, S.H. and Joshi, S., 2003, CFD validation for a marine propeller using a unstructured mesh based RANS method, FEDSM03, Honolulu, USA.

Rumsey, C.L. and Spalart, P.R., 2008, Turbulence model behavior in low reynolds number regions of aerodynamic flowfields, 38th AIAA Fluid Dynamics Conference and Exhibit, Seattle, WA.

Shin, T.H., Liou, W.W., Shabir, A. and Zhu, J., 1995, A new $k - \varepsilon$ eddy viscosity model for high reynolds number turbulent flows model development and validation, Computers and Fluids, Vol. 24, No. 3, pp. 227-238.

Simonsen, C.D. and Stern, F., 2005, RANS maneuvering simulation of Esso Osaka with rudder and a body-force propeller, Journal of Ship Research, Vol. 49, No. 2.

Smith, A.M.O. and Cebeci, T., 1967, Numerical solution of the turbulent boundary layer equations, Douglas aircraft division report DAC 33735.

Spalart, P.R. and Allmaras, S.R., 1992, A one-equation turbulence model for aerodynamic flows, AIAA paper 92-0439.

Speziale, C.G., Sarkar, S. and Gatski, T.B., 1991, Modelling the pressure-strain correlation of turbulence: an invariant dynamical systems approach, J. Fluid Mechanics, Vol. 277, pp. 245-272.

Wang, T., Zhou, L.D. and Zhang, X., 2003, Numerical simulation of 3-D viscous flow field around axisymmetric body with integrated ducted propulsion, J. of Ship Mechanics, Vol. 7, No. 2.

Wilcox, D.C., 1988, Re-assessment of the scale-determining equation for the advanced turbulence models, AIAA Journal, Vol. 26, pp. 1414-1421.